

Observing the Earth's Plasmasphere and Ionosphere From the Lunar Surface

Original

Observing the Earth's Plasmasphere and Ionosphere From the Lunar Surface / Cesaroni, C., Spogli, L., Guerra, M., Ghidoni, R., Ventriglia, V., Minetto, A., Nardin, A., Alfonsi, L., Dosis, F.. - In: GEOPHYSICAL RESEARCH LETTERS. - ISSN 0094-8276. - ELETTRONICO. - 53:12(2026). [10.1029/2026gl121811]

Availability:

This version is available at: 11583/3012290 since: 2026-06-20T13:50:11Z

Publisher:

Wiley

Published

DOI:10.1029/2026gl121811

Terms of use:

This article is made available under terms and conditions as specified in the corresponding bibliographic description in the repository

Publisher copyright

(Article begins on next page)

Geophysical Research Letters[®]

RESEARCH LETTER

10.1029/2026GL121811

Observing the Earth's Plasmasphere and Ionosphere From the Lunar Surface



Key Points:

- LuGRE allows the unprecedented characterization of Earth's plasma environment using GNSS signals tracked from the lunar surface
- Observations in the topside ionosphere/plasmasphere transition region reveal that dayside plasma density is significantly lower than modeled
- Nightside observations during a minor storm show higher-than-predicted bulge or F-layer densities

Correspondence to:

C. Cesaroni,
claudio.cesaroni@ingv.it

Citation:




Cesaroni, C., Spogli, L., Guerra, M., Ghidoni, R., Ventriglia, V., Minetto, A., et al. (2026). Observing the Earth's plasmasphere and ionosphere from the lunar surface. *Geophysical Research Letters*, 53, e2026GL121811. <https://doi.org/10.1029/2026GL121811>

Received 12 JAN 2026

Accepted 2 JUN 2026

Author Contributions:

Conceptualization: C. Cesaroni, L. Spogli, A. Minetto, L. Alfonsi, F. Dovis
Data curation: M. Guerra, V. Ventriglia, A. Minetto, A. Nardin
Formal analysis: M. Guerra, R. Ghidoni, L. Alfonsi
Funding acquisition: L. Alfonsi, F. Dovis
Investigation: R. Ghidoni
Methodology: C. Cesaroni, L. Spogli, R. Ghidoni, V. Ventriglia, A. Minetto, A. Nardin, L. Alfonsi, F. Dovis
Software: M. Guerra, R. Ghidoni, V. Ventriglia
Supervision: C. Cesaroni
Visualization: M. Guerra, V. Ventriglia
Writing – original draft: C. Cesaroni, L. Spogli
Writing – review & editing: C. Cesaroni, L. Spogli, M. Guerra, R. Ghidoni, V. Ventriglia, A. Minetto, A. Nardin, L. Alfonsi, F. Dovis

C. Cesaroni¹ , L. Spogli¹ , M. Guerra¹ , R. Ghidoni¹, V. Ventriglia¹ , A. Minetto² , A. Nardin² , L. Alfonsi¹ , and F. Dovis²

¹Istituto Nazionale di Geofisica e Vulcanologia, Rome, Italy, ²Politecnico di Torino, Turin, Italy

Abstract We present the analysis of the first lunar-based observational characterization of the Earth's plasmasphere and ionosphere using Global Navigation Satellite Systems signals tracked from the lunar surface by the Lunar GNSS Receiver Experiment (LuGRE). The Earth-Moon geometry enables limb sounding of the plasmasphere at altitudes exceeding 3,000 km, bridging a critical observational gap. We compared Total Electron Content measurements from GPS and Galileo satellites' signals with predictions from the Global Core Plasma Model. While the model captures the general morphology of the plasmasphere, significant discrepancies emerge in the ionosphere/plasmasphere transition region. Specifically, LuGRE data reveal an overestimation of electron density by the model during the dayside phase indicating a lower plasma refilling efficiency than currently parameterized and an underestimation during the nightside phase. These results demonstrate the capability of lunar-based GNSS measurements to continuously monitor the global plasma environment, paving the way for future permanent observatories on the Moon.

Plain Language Summary Earth is surrounded by a layer of charged particles called the ionosphere/plasmasphere. This system impacts “space weather,” which can disrupt satellites and communications. However, a major “blind spot” exists between our atmosphere and deep space that is difficult to measure from Earth or low-orbiting satellites. The LuGRE mission addressed this by placing a GNSS receiver on the Moon. Unlike Earth-based sensors, LuGRE looked back at our planet, measuring plasma density across that blind spot as signals traveled toward the Moon. Our results showed significant disagreements with standard models, proving current maps of Earth's space environment are inaccurate. This confirms the Moon is an ideal location for a permanent observatory to monitor space weather and protect vital technology.

1. Introduction

The Earth's ionosphere/plasmasphere boundary actively drives geospace dynamics rather than passively receiving solar activity (Usanova & Shprits, 2017). This coupled system acts as the primary reservoir of cold plasma for the inner magnetosphere, ejecting particles globally (Chappell, 1988). Outflows include the supersonic light H⁺ and He⁺ polar wind (Banks & Holzer, 1969) and energetic auroral O⁺ ions that contribute to magnetospheric circulation (Chappell et al., 2021; Lotko, 2007).

These populations are fundamental to magnetospheric-ionospheric coupling, potentially sourcing the entire magnetosphere (Chappell et al., 1987; Delzanno et al., 2021). As cold ions (~1 eV) move upward, they transport through magnetotail lobes and energize via curvature and gradient drifts (Chappell et al., 2021; Huddleston et al., 2005). This process mass-loads the plasma sheet, altering Alfvén speeds and potentially triggering substorms (Chappell et al., 2021; Lotko, 2007). Furthermore, this plasma distribution governs radiation belt wave-particle interactions (Ripoll et al., 2023; Usanova & Shprits, 2017). High-density regions favor hiss waves (creating the slot region), while low-density regions facilitate chorus wave excitation, the primary mechanism for accelerating relativistic electrons (Delzanno et al., 2021; Ripoll et al., 2023).

Despite its importance (Budden, 1988; Davies, 1990; Rawer, 2013), cold plasma characterization suffers from heterogeneous measurements and coverage gaps (Ripoll et al., 2023; Smirnov et al., 2025). A primary constraint is the observational gap between 800 and 8,000 km, the transition region between ionospheric and plasmaspheric populations (Padokhin et al., 2025; Smirnov et al., 2025). Although ground-based Incoherent Scatter Radars (ISRs) can successfully probe the topside ionosphere deep into this transition region, reaching altitudes of 2,500 km at Arecibo and over 5,000 km at Jicamarca, such observations are geographically restricted to a few sites and are not continuously available (e.g., Garzon et al., 2011; Hysell et al., 2017). On a global scale, a ctive

© 2026. The Author(s).

This is an open access article under the terms of the [Creative Commons Attribution License](https://creativecommons.org/licenses/by/4.0/), which permits use, distribution and reproduction in any medium, provided the original work is properly cited.

profiling like GNSS Radio Occultation (RO) is confined below 800 km, while magnetospheric missions generally derive electron density from Upper Hybrid Resonance (UHR) frequencies only above ~ 2 Earth radii (RE) (Menk et al., 2014; Smirnov et al., 2025). While missions such as ISEE, CRRES, Polar, IMAGE, and the Van Allen Probes focused on high altitudes (Chu et al., 2017; Smirnov et al., 2025; Zhelavskaya et al., 2017), JAXA's Arase and Akebono, alongside Cluster II analysis pipelines, have begun bridging this divide (Gilet et al., 2021; Kitamura et al., 2009; Kumamoto et al., 2018; Miyoshi et al., 2018). Nevertheless, current empirical models describe the global environment unevenly (Smirnov et al., 2025; Watanabe et al., 2025).

These blind spots significantly impact GNSS and satellite communications, where Plasmaspheric Electron Content (PEC) can account for 60% of nighttime signal delays (Jakowski & Hoque, 2018; Jin et al., 2021). Empirical models like NeQuick systematically underestimate PEC during low solar activity (Kashcheyev & Nava, 2019; Pignalberi et al., 2025). Although optimization techniques utilizing RO and Precise Orbit Determination (POD) Total Electron Content (TEC) exist, they remain constrained by Low Earth Orbit (LEO) altitudes and boundary ambiguity (González-Casado et al., 2015; Pignalberi et al., 2025).

The Lunar GNSS Receiver Experiment (LuGRE) is a joint NASA–ASI initiative that flew a GNSS receiver aboard the Firefly *Blue Ghost* lander, which launched in January 2025 and successfully landed on the Moon in March 2025, thereby providing a novel solution (Parker et al., 2022, 2026). Data collected by LuGRE (Freeman, 2025; Parker et al., 2025) capture terrestrial signals propagating nearly-horizontally over paths exceeding 3,000 km, in contrast to the predominantly vertical geometry of ground-based measurements (Iiyama & Gao, 2025; Minetto et al., 2022). This geometry makes LuGRE observations exceptionally sensitive to PEC, providing a powerful probe to resolve modeling underestimations (Iiyama & Gao, 2025; Pignalberi et al., 2025). In this paper, we demonstrate LuGRE's capability to bridge the global inner magnetosphere observational gap by characterizing electron density (Gallagher et al., 2000; Iiyama & Gao, 2025). Specifically, we analyze discrepancies between LuGRE-measured TEC and the Global Core Plasma Model (GCPM; Gallagher et al., 2000).

2. Data and Methods

2.1. LuGRE GNSS Receiver and Data Acquisition

LuGRE, utilized a custom-designed GNSS payload developed by Qascom. The core hardware is the QN400-SPACE GNSS receiver, a Software Defined Radio (SDR) modular unit (Parker et al., 2026). It consisted of a radio frequency front-end and a baseband processor that captured and digitally processed L1/L5 and E1/E5a signals from Global Positioning System (GPS) and Galileo, respectively. The SDR implementation provided dynamic tracking-resource allocation and adaptive parameter reconfiguration across mission phases, enabling operation under extreme lunar orbiting dynamics and signal attenuation.

The payload generated and downlinked three primary data products for scientific investigation: (a) onboard Position, Velocity, and Timing solutions; (b) raw GNSS observables (pseudorange, Doppler shift, and carrier-to-noise density ratio) obtained during real-time operations and leveraged for the present work; and (c) snapshots of baseband digital signal samples, referred to as In-phase and Quadrature samples.

In 2025, LuGRE collected data during spacecraft commissioning (15–16 January), transit (17 January to 12 February), lunar orbiting (14–27 February), and throughout a 12-day surface operation campaign (3–16 March) at Mare Crisium landing site (18.56°N, 61.81°E, selenographic coordinates). Overall, LuGRE performed 16 nearly one-hour operations while in flight to the Moon, including 2 for commissioning, 9 in the Earth-centered phasing loops, and 5 in lunar orbit. LuGRE operated for a cumulative time of more than 111 hr and spent more than 106 hr performing real-time processing. The majority of LuGRE operating time was on the lunar surface, where it successfully operated nearly 93 hr across nine operations, including over 3 hr past the beginning of lunar sunset.

Operating beyond 60 Earth radii, the receiver must contend with severe signal attenuation, with carrier-to-noise density ratio (C/N_0) levels dropping well below those typical of terrestrial applications and exhibiting pronounced fluctuations as satellites approach the Earth's limb, attributed to propagation through ionized atmospheric layers, as further investigated in this work.

Thanks to a small antenna pointing error, surface operations provided a favorable geometry for Earth observation compared to other mission phases. Continuous long-duration surface operation enabled the acquisition of an

extensive data set spanning a wide range of ionospheric and plasmaspheric crossings, driven by the evolving relative geometry between multiple satellites and the landing site. Moreover, prolonged uninterrupted surface operations allowed the on-board oscillator to reach steady-state stability, enhancing acquisition robustness and enabling continuous measurements from a larger number of satellites compared to in-flight ones.

The data used in this study consists of multi-frequency (i.e., L1/L5 and E1/E5a) carrier pseudorange measurements from the GPS and Galileo satellites, acquired during the real-time operations performed by the receiver on lunar surface with a measurement output rate of 1 Hz associated with the main-lobe portion of the satellites' antenna radiation patterns. The availability of multi-frequency observations enables their combination for the estimation of the TEC along the ray paths crossing both ionosphere and plasmasphere regions. We identified the 3–4 March and 14–16 March 2025 acquisition windows as optimal for characterizing the plasma environment, as they allow for probing diverse ionospheric-plasmaspheric regions across multiple longitudinal sectors and geomagnetic conditions.

2.2. Derivation of TEC

The derivation of TEC from GNSS observables is a cornerstone of ionospheric remote sensing, exploiting the dispersive nature of plasma inducing phase advance and group delay on dual-frequency signals. In the case of LuGRE, which tracks GPS (L1/L5) and Galileo (E1/E5a) transmissions at lunar distances, this approach provides measurements of integrated electron density along exceptionally long ray paths that propagate quasi-horizontally through the Earth's ionosphere and plasmasphere. Compared to conventional ground-based or LEO-based TEC estimation, LuGRE's unique observation geometry enables sensing the plasma environment at unprecedented altitudes (>1,000 km). At these heights, the relative contribution of the plasmasphere to TEC becomes more significant, particularly during nighttime conditions or periods of low solar activity.

LuGRE's raw GNSS observables enable continuous observation arcs typically lasting between 10 and 60 min per satellite. TEC retrieval from carrier-phase observations exploits the frequency-dependent response of GNSS signals to plasma density, using dual-frequency pairs (L1/L5 for GPS and E1/E5a for Galileo). Specifically, the Geometry-Free Linear Combination (GFLC) of carrier-phase observables is formed to eliminate geometric range, clock errors, and tropospheric delays, isolating the dispersive ionospheric contribution. The GFLC is defined as:

$$\text{GFLC} = \left(\frac{1}{A}\right) \left(\frac{f_1^2 f_2^2}{f_1^2 - f_2^2}\right) (L_1 \lambda_1 - L_2 \lambda_2), \quad (1)$$

where $A = 40.308 \text{ m}^3 \text{ s}^{-2}$, L_1 and L_2 are the carrier-phase measurements expressed in cycles, λ_1 and λ_2 are the corresponding signal wavelengths, and f_1 and f_2 are the carrier frequencies. The resulting quantity is conventionally expressed in TEC units (TECu), with $1 \text{ TECu} = 10^{16} \text{ electrons m}^{-2}$.

Carrier-phase-derived GFLC estimates exhibit very low measurement noise, making them suitable for resolving small-to large-scale ionospheric and plasmaspheric variability, especially at temporal resolutions such as 1 s. In this data set, the residual TEC noise level, estimated using the median absolute deviation (MAD), is approximately 0.03 TECu, confirming the high precision of the carrier-phase measurements. However, carrier-phase observables are affected by an unknown integer phase ambiguity and interfrequency bias that remain constant over continuous observation arcs, provided that no cycle slips or losses of lock occur. As a result, absolute TEC values cannot be directly retrieved from phase measurements alone, since each continuous arc is shifted by an unknown constant bias that is typically addressed through calibration procedures (see, e.g., Cesaroni et al., 2021 and references therein). Despite this limitation, the raw GFLC time series within each continuous arc retains physical meaning and can be robustly analyzed in terms of relative temporal variations, even when the absolute TEC level is not resolved. In this study, the GFLC was roughly calibrated arc-wise by setting its lowest value equal to the lowest value obtained from the ionosphere-plasmasphere model. Where the plasma density is minimal, the model error should also be minimal, allowing for a better comparison of the time evolution of measured and modeled TEC. In addition, to mitigate residual phase-related discontinuities, phase jumps producing apparent TEC variations larger than 3 TECu s^{-1} were flattened, while data gaps were filled using linear interpolation based on the 30 samples preceding each gap.

2.3. The Global Core Plasma Model (GCPM)

The GCPM is an empirical framework designed to provide a spatially continuous description of electron density and ion composition throughout the inner magnetosphere (Gallagher et al., 2000). The model is constructed by integrating region-specific sub-models, encompassing the ionosphere, plasmasphere, plasmopause, magnetospheric trough, and polar cap, joined by hyperbolic tangent functions that ensure the resulting distribution is continuous in both value and gradient (Gallagher et al., 2000; Wu et al., 2015). The GCPM is driven by different parameters, such as the geomagnetic activity index (Kp), the solar radio flux (F10.7), the annual mean sunspot number, and the day-of-year (Gallagher et al., 2000; Iiyama & Gao, 2025). For its lower boundary, the model incorporates the International Reference Ionosphere (IRI) to represent ionospheric densities, while the inner plasmasphere is described by an exponential density fall-off relative to the L-shell (Bilitza et al., 2024; Gallagher et al., 2000). A defining feature of the GCPM is the inclusion of a blunt plasmaspheric bulge that rotates sunward and contracts as geomagnetic activity increases. Beyond total electron density, the model provides the relative concentrations of major ions, such as H⁺, He⁺, and O⁺, particularly within the plasmasphere.

The scientific community has widely adopted the GCPM as a standard reference for characterizing typical core plasma conditions (Ripoll et al., 2023; Wu et al., 2015). Most recently, the GCPM has been instrumental in the delay characterization studies for Lunar GNSS receivers (Iiyama & Gao, 2025), and we decided to adopt the same model to be consistent with their approach. To quantify the plasma contribution along the signal path between the Earth-orbiting GPS or Galileo satellites and the Moon-based LuGRE receiver, a dedicated numerical integration framework was developed. This implementation translates the empirical density profiles provided by the GCPM v2.4 into TEC values using a numerical integration along the line of sight. The signal path is modeled as a simple vector $R_{\text{sat-moon}} = P_{\text{moon}} - P_{\text{sat}}$, where P_{sat} represents the GPS or Galileo satellite position and P_{moon} represents the LuGRE receiver on the lunar surface (Mare Crisium). To optimize the integration, the algorithm identifies the specific segment of the vector that traverses the Earth's plasma environment between a lower altitude boundary R_1 , defined as the radius of the Earth, and an upper boundary R_2 , set at the Earth radius plus 40,000 km. This specific range was selected because it encompasses the regions where the highest concentration of electrons is expected, effectively capturing the bulk of the ionospheric and plasmaspheric contributions. Only the sub-segment where the path is within this specified spherical crown is considered for electron content accumulation, while the remaining part of the signal path is considered to have no contribution.

The simulation was performed specifically for the time windows of available LuGRE observations, utilizing a temporal resolution of 30 s. This resolution was selected to provide sufficient granularity to capture small plasma variations while maintaining computational efficiency. Furthermore, increasing the temporal resolution beyond this point would not yield significantly more accurate results, as the empirical nature of the underlying model limits the precision of the output at higher frequencies. The TEC is calculated by evaluating the integral of the electron density ρ along the ray path $R_{\text{sat-moon}}$ and can be expressed as $\text{TEC} = \int_{R_{\text{sat-moon}}} \rho(s) ds$. In our implementation, the integral is approximated using a discrete summation over 1,000 steps within the valid segment.

2.4. Observational Geometry

The observational geometry of the LuGRE experiment is governed by the Moon's synodic orbital motion, which determines the receiver's position relative to the Earth's magnetosphere. As illustrated in Figure 1, the lunar receiver transitions between distinct plasma environments depending on the lunar phase. During the full moon phase, the Moon resides deep within the Earth's magnetotail (Figure 1a), allowing LuGRE to probe the extended plasmasphere, plasma sheet, and tail lobes shielded from the direct solar wind. Conversely, during the new moon phase, the Moon is positioned upstream in the solar wind (Figure 1b), where the signal path traverses the bow shock, magnetosheath, and the compressed dayside magnetosphere (Halekas et al., 2018).

As detailed in Section 2.1, the GNSS acquisition windows selected for plasma characterization occur during the waxing crescent phase (3–4 March 2025) and the full moon (14–16 March 2025). To exemplify the observational geometry, we report on two specific case studies representing these contrasting magnetosphere-Moon relative positions, as visualized in Figure 2. Specifically, Figure 2a displays the electron density along ray paths modeled with the GCPM for the nightside/magnetotail case: satellite G24 is tracked between 20:50 and 21:58 UTC on 14 March 2025 (lunar phase ~99.7%), where the receiver is immersed in the magnetotail. Figure 2b displays the dayside/upstream case: Galileo satellite E02 is tracked between 06:52 and 08:00 UTC on 3 March 2025 (lunar phase ~14.7%), where the receiver is located outside the magnetosphere.

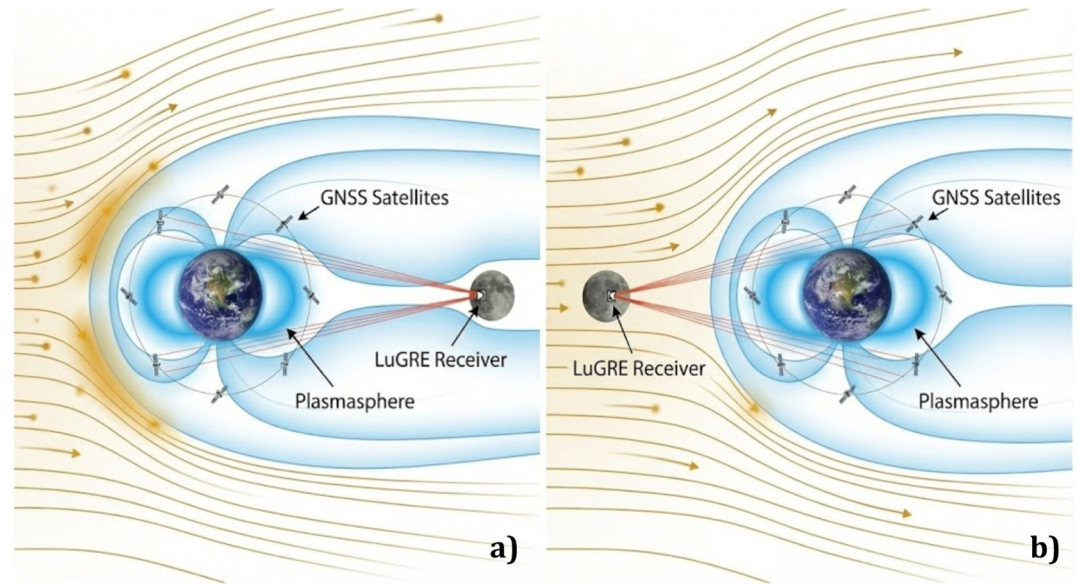


Figure 1. Schematic representation of the LuGRE observational geometry within the Earth-Moon plasma environment (not to scale). (a) Configuration during the lunar passage through the Earth's magnetotail (nightside). The signal ray paths (red lines) traverse the plasmasphere and the magnetosphere tangentially, sampling the plasmaspheric bulge, the plasma sheet, and the tail lobes. (b) Configuration during the lunar dayside phase, where the Moon is positioned upstream in the solar wind. In this geometry, GNSS signals traverse the compressed dayside magnetosphere, the magnetosheath, and the bow shock before reaching the lunar surface. The solar wind (yellow arrows) shapes the magnetospheric cavity, confining the GNSS constellation within the magnetopause while the LuGRE receiver operates in the interplanetary medium (generated with Gemini Nano Banana Pro tool).

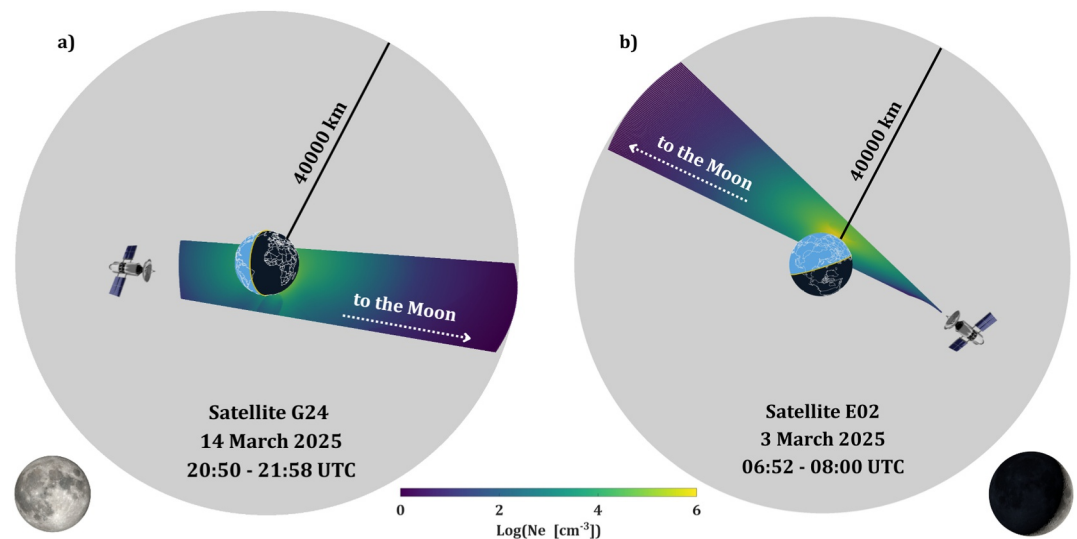


Figure 2. Schematic representation of the signal propagation path from a GNSS satellite to the receiver located on the lunar surface. The color scale represents the electron plasma density modeled using the GCPM, while the gray spherical boundary indicates a distance of 40,000 km from the reference Earth's surface, representing the maximum extent of the model's domain used in this paper. The direction of the Moon is indicated in each panel together with the lunar phase (small pictures at the bottom of each panel). (a) Nightside geometry where the Moon is located within the magnetosphere, tracking GPS satellite G24 between 20:50 and 21:58 UTC on 14 March 2025. (b) Dayside geometry (Moon sunward of Earth) tracking Galileo satellite E02 between 06:52 and 08:00 UTC on 3 March 2025.

It is worth remembering that we use the GCPM to calculate plasma density up to a distance of 40,000 km from the Earth's surface, indicated by the boundary of the gray sphere in Figure 2. Beyond that boundary, we assume a zero density for the purpose of the integrated content calculation. This assumption is justified by the tenuous nature of the solar wind and magnetosheath plasma ($N_e \sim 5\text{--}10\text{ cm}^{-3}$). Even integrated over the remaining lunar distance, their contribution typically remains below 1 TECu, which is negligible for our purposes.

These GNSS signal ray paths traverse the Earth's plasmasphere and ionosphere as low as the E-layer region, as it will be also demonstrated in Section 3. While ionospheric refraction typically necessitates ray-bending corrections for precise positioning, recent simulations comparing the total path length and electron content between a full ray-tracing solution and a geometric straight line indicate that the difference in path position at ionospheric heights remains below 5 km (Iiyama & Gao, 2025). Given the ultra-long baseline of the Earth-Moon link, this deviation is considered negligible for the purpose of the proposed analysis. Therefore, a straight-line propagation approximation is adopted as a first-order approximation of the propagation geometry, sufficient to capture both the plasmaspheric densities and the morphological transition to the ionosphere and its lower part.

3. Results

Figure 3 presents four representative observation arcs involving Galileo and GPS satellites, selected to illustrate LuGRE's capability to resolve both vertical plasma structures and longitudinal variations. The GCPM is superimposed on the measured data to provide a baseline for the expected modulation of the TEC. In all observations, the TEC time series are aligned at their lowest values: where density is lowest and absolute model errors are minimized. This is evidenced by the coinciding TEC values at the beginning or end of the tracks in Figure 3.

The first two cases, involving Galileo satellites E02 and E26 on 3 March 2025, mainly probe the vertical structure of the dayside and nightside plasmasphere, respectively. These observations occurred approximately three days after a minor geomagnetic storm ($Dst \sim -40$ nT on February 28th), allowing for a significant plasma refilling under quiet conditions ($K_p \leq 2+$ throughout the entire day before the observation). For satellite E02 (Figures 3a and 3b), the signal tangent point descends from high plasmaspheric altitudes ($>3,000$ km) to a perigee of ~ 800 km before ascending again. While the modeled TEC (black curve) tracks the general morphology of the measure (red curve), a significant discrepancy is observed in the transition region. The model predicts a peak density at almost 50 TECu, whereas the observations reveal a much more moderate peak of ~ 40 TECu. This ~ 10 TECu deficit suggests that the dayside plasma reservoir in the 800–3,000 km transition region is considerably less dense than climatological parameters indicate, implying a lower efficiency of ionospheric refilling or a different scale height for light ions.

Conversely, the observation of satellite E26 (Figures 3c and 3d) samples a higher-altitude regime, with the tangent point remaining above 2,200 km. In this “pure plasmasphere” geometry, the absolute magnitude of the measured TEC aligns more closely with the model. However, the LuGRE data captures distinct fine-scale density variations, such as the localized enhancement near 12:53 UT, that are absent in the smooth model prediction, demonstrating the instrument's sensitivity to small-scale plasmaspheric irregularities.

The bottom two rows, displaying GPS satellites G24 and G30 on late 14 and early 15 March 2025 highlight strong longitudinal asymmetries during the nightside phase. The observation of satellite G24 (Figures 3e and 3f) over the Pacific sector exhibits a morphological agreement between the model and measurements, with the LuGRE data showing a higher peak (~ 200 TECu) compared to the GCPM (~ 130 TECu). This confirms that, in this longitudinal sector, the model captures the general state of the plasmasphere reasonably well even if, as in the previous cases, the measurements show a fine structure of the electron density in the plasmasphere that is not captured by the model. This is particularly true moving from low to high latitudes passing through the F region altitudes (~ 300 km at 21:25 UT) and the transition region ($\sim 900\text{--}1,000$ km at 21:35–21:40 UT). It is worth noting that such high absolute Slant TEC values are a direct physical consequence of the limb-sounding geometry; as the signal traverses the dense F-region horizontally over thousands of kilometers, it experiences a massive geometric amplification compared to standard vertical observations.

The observation of GPS satellite G30 (Figures 3g and 3h), traversing the African and South Atlantic longitudinal sectors, presents a distinct contrast to the Pacific sector observations. While the GCPM generally reproduces the temporal morphology of the tracking arc, it quantitatively underestimates the TEC measured by LuGRE, particularly during the pre-perigee phase of the observation. The measured TEC values in the left peak of the

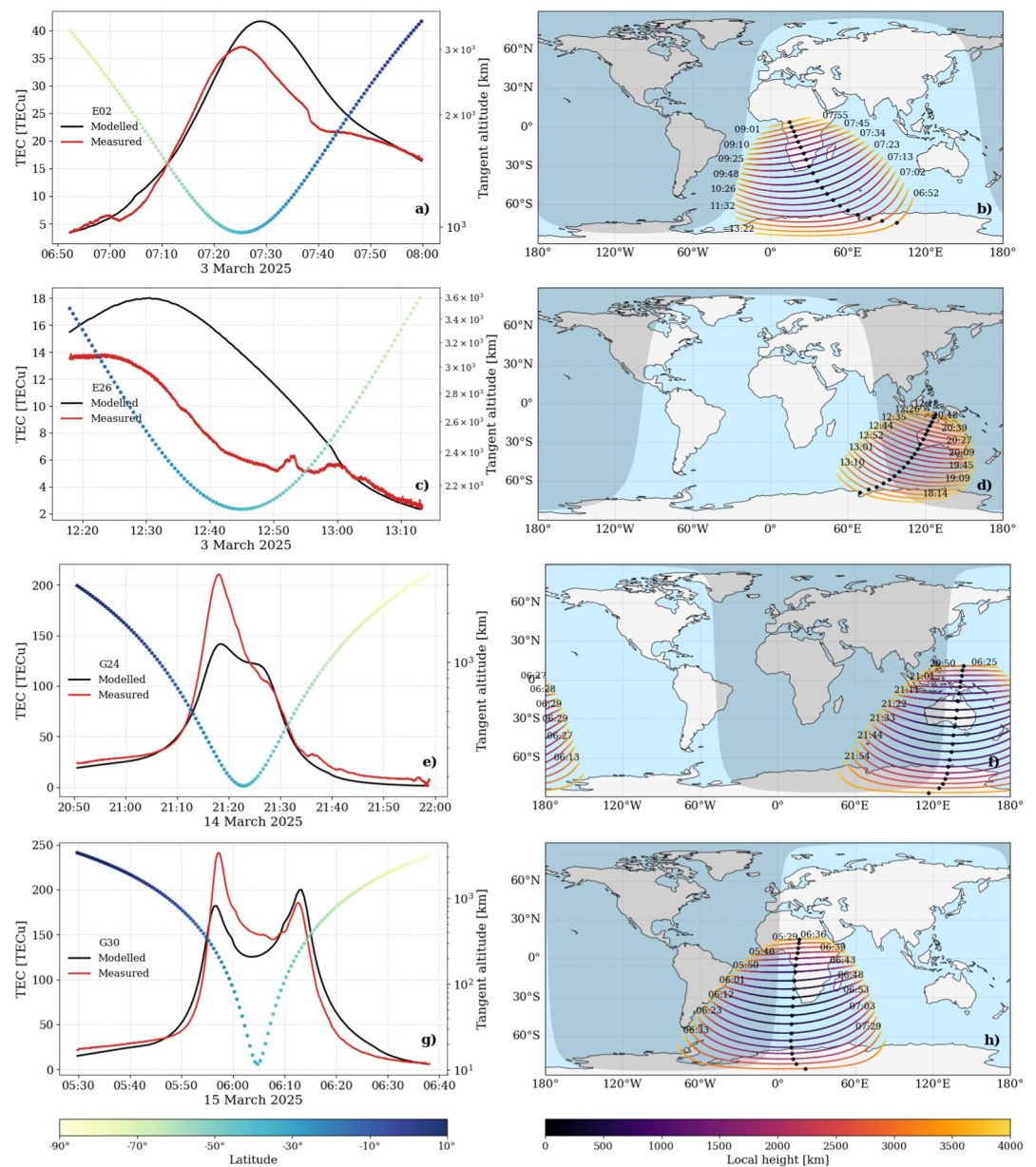


Figure 3. Comparison of LuGRE-measured versus GCPM-modeled TEC for four representative GNSS tracking arcs. (Panels a, c, e, g) Temporal evolution of Slant TEC for satellites Galileo E02 and E26 (3 March) and GPS G24 and G30 (14 and 15 March, respectively). The red curves indicate LuGRE measurements, while the black curves show the GCPM model predictions. The superimposed multi-colored scatter plot represents the ray path tangent point altitude (right axis), color-coded by latitude. (Panels b, d, f, h) Corresponding geographical projections of the signal ray paths. The tracks are color-coded by local tangent point altitude, with blue dots marking the location of minimum altitude (perigee). The gray shaded regions indicate the Earth's nightside.

profile (Figure 3g), corresponding to a “low-latitude” ray-path, exceed the model predictions of ~ 60 TECu. This discrepancy suggests that the plasma refilling rates or the field-aligned density distribution in the plasmaspheric bulge region may be more robust than currently parameterized in the GCPM for these geomagnetic conditions ($K_p = 4-$, but during a minor geomagnetic storm) or a possible mismodeling of the ionospheric F layer dominating at the altitude of the tangent point (200–300 km).

Morphologically, both the modeled and measured TEC profiles exhibit a characteristic ‘saddle’ shape centered around the time of closest approach ($\sim 06:00$ UTC). This feature is driven by the specific geometry of the

observation: as indicated by the color-coded altitude scatter plot, the signal tangent point descends to altitudes below 300 km. Consequently, the line-of-sight penetrates the peak of the F-layer and traverses the E-region, resulting in a local minimum in the integrated content before the path ascends again through the denser layers. The difficulty of the IRI in accurately modeling the bottom-side electron density profile at low-latitudes during a geomagnetic storm (even if a minor one) contributes to the residuals observed in the pre-perigee observations (~05:55 UT). This will be further assessed by considering the data assimilation schemes recently introduced by many authors (see e.g. Bilitza et al., 2024; Pignalberi et al., 2025).

Furthermore, observations highlight the topological boundaries of the Earth's plasma environment. The measurements clearly distinguish between plasmaspheric and extra-plasmaspheric regimes based on latitude. The low TEC values observed at high altitudes when the ray path traverses high latitudes (yellow/green points in the scatter plots), contrasted with higher values at low latitudes, are consistent with the absence of the plasmasphere in the polar regions. This confirms LuGRE's ability to detect the transition from the dense, closed field lines of the plasmasphere to the tenuous, open field lines characteristic of the high-latitude lobes.

4. Conclusions

This study presents the first direct characterization of the Earth's plasmasphere and ionosphere using GNSS signals tracked from the lunar surface. By exploiting the unique Earth-Moon geometry, the LuGRE experiment has successfully bridged the longstanding observational gap in the topside ionosphere/plasmasphere transition region, a domain that is difficult to profile continuously with Low Earth Orbit satellites or ground-based techniques.

Our comparison of the measured TEC with the GCPM reveals the dayside plasma reservoir in the transition region is significantly less dense than climatologically predicted, suggesting that the diffusive equilibrium scale heights or ionospheric refilling rates currently parameterized in empirical models may be overestimated. Furthermore, LuGRE has demonstrated the capability to perform deep vertical sounding down to E-region altitudes. The detection of a characteristic “saddle” morphology in the TEC profiles confirms the instrument's ability to probe the bottomside ionosphere as well. Additionally, the sharp contrast between high-latitude and low-latitude measurements validates the geometric boundary of the plasmasphere, clearly distinguishing the dense inner region from the tenuous high-latitude lobes.

The results presented here demonstrate that the lunar surface offers an unrivaled vantage point for “outside-in” sounding of the terrestrial magnetosphere. While LuGRE has provided a proof-of-concept using opportunistic GNSS signals, future lunar exploration enables the transition from sporadic measurement to continuous, global monitoring.

A permanent lunar-based radio observatory could fundamentally advance our understanding of plasmaspheric dynamics by enabling purely plasmaspheric tomography, overcoming the limitations of the combined topside ionosphere/plasmasphere tomography available at present (Gerzen & Minkwitz, 2026). By combining the Moon's monthly orbital precession with the Earth's daily rotation, a continuously operating receiver could systematically scan all local time sectors and latitudes. This would allow for the 4D reconstruction of plasma density structures, resolving long-standing questions regarding the erosion of the plasmasphere during geomagnetic storms and the subsequent refilling rates of flux tubes over solar cycle timescales.

Conflict of Interest

The authors declare no conflicts of interest relevant to this study.

Availability Statement

LuGRE raw data are available at Parker et al. (2025) <https://doi.org/10.5281/zenodo.16411687>. Geometry Free Linear Combination of the GNSS observables used in this paper are available at Guerra (2026). The Kp data used in this paper are available at Matzka et al. (2021). Python code (including the Python version of the GCPM model) for the data analysis and visualization is available at Ventriglia et al. (2026).

Acknowledgments

This study was partly funded within the contract n. 2.021-26-HH.0 between Agenzia Spaziale Italiana and Politecnico di Torino "Attività di Ricerca e Sviluppo inerente alla Navigazione GNSS nello Space volume Terra/Luna nell'ambito del Lunar GNSS Receiver Experiment". Special thanks to Giordiana De Franceschi and Vincenzo Romano for fruitful discussions and the "CENTRO OSSERVAZIONI SPAZIALI DELLA TERRA" (<https://cos.ingv.it/>) of the INGV for the supporting framework. The authors thank Matthew James for providing the Python version of the GCPM model. Open access publishing facilitated by Istituto Nazionale di Geofisica e Vulcanologia, as part of the Wiley - CRUI-CARE agreement.

References

- Banks, P. M., & Holzer, T. E. (1969). High-latitude plasma transport: The polar wind. *Journal of Geophysical Research*, *74*(26), 6317–6332. <https://doi.org/10.11575/PRISM/41728>
- Bilitza, D., Truhlik, V., Yoshihara, O., & Moldwin, M. B. (2024). Development and improvement of the international reference ionosphere with special emphasis on the topside and extension to the plasmasphere. *Annals of Geophysics*, *67*(4). <https://doi.org/10.4401/ag-9145>
- Budden, K. G. (1988). *The propagation of radio waves: The theory of radio waves of low power in the ionosphere and magnetosphere*. Cambridge University Press.
- Cesaroni, C., Spogli, L., & De Franceschi, G. (2021). IONORING: Real-time monitoring of the total electron content over Italy. *Remote Sensing*, *13*(16), 3290. <https://doi.org/10.3390/rs13163290>
- Chappell, C. R. (1988). The terrestrial plasma source: A new perspective in solar-terrestrial processes from dynamics explorer. *Reviews of Geophysics*, *26*(2), 229–248. <https://doi.org/10.1029/RG026i002p00229>
- Chappell, C. R., Glocer, A., Giles, B. L., Moore, T. E., Huddleston, M. M., & Gallagher, D. L. (2021). The key role of cold ionospheric ions as a source of hot magnetospheric plasma and as a driver of the dynamics of substorms and storms. *Frontiers in Astronomy and Space Sciences*, *8*, 746283. <https://doi.org/10.3389/fspas.2021.746283>
- Chappell, C. R., Moore, T. E., & Waite, J. H., Jr. (1987). The ionosphere as a fully adequate source of plasma for the earth's magnetosphere. *Journal of Geophysical Research*, *92*(A6), 5896–5910. <https://doi.org/10.1029/JA092iA06p05896>
- Chu, X., Bortnik, J., Li, W., Ma, Q., Denton, R., Yue, C., et al. (2017). A neural network model of three-dimensional dynamic electron density in the inner magnetosphere. *Journal of Geophysical Research: Space Physics*, *122*(9), 9183–9197. <https://doi.org/10.1002/2017JA024464>
- Davies, K. (1990). Ionospheric radio. <https://doi.org/10.1049/pbew031e>
- Delzanno, G. L., Borovsky, J. E., Henderson, M. G., Resendiz Lira, P. A., Roytershteyn, V., & Welling, D. T. (2021). The impact of cold electrons and cold ions in magnetospheric physics. *Journal of Atmospheric and Solar-Terrestrial Physics*, *220*, 105599. <https://doi.org/10.1016/j.jastp.2021.105599>
- Freeman, R. H. (2025). Lunar surface operations: On the science investigations of blue Ghost-1 payloads. *Journal of Space Operations & Communicator*, *21*(2).
- Gallagher, D. L., Craven, P. D., & Comfort, R. H. (2000). Global core plasma model. *Journal of Geophysical Research*, *105*(A8), 18819–18833. <https://doi.org/10.1029/1999JA000241>
- Garzon, D. P., Brum, C. G. M., Echer, E., Aponte, N., Sulzer, M. P., Gonzalez, S. A., et al. (2011). Response of the topside ionosphere over arcicbo to a moderate geomagnetic storm. *Journal of Atmospheric and Solar-Terrestrial Physics*, *73*(11–12), 1568–1574. <https://doi.org/10.1016/j.jastp.2011.02.016>
- Gerzen, T., & Minkwitz, D. (2026). Simultaneous multiplicative column-normalized method with time propagation (4DSMART+) for 4D tomography of topside ionosphere and plasmasphere in comparison with NeQuick and SMART+. *Advances in Space Research*, *77*(5), 6280–6294. <https://doi.org/10.1016/j.asr.2025.12.113>
- Gilet, N., De Leon, E., Gallé, R., Vallières, X., Rauch, J. L., Jegou, K., et al. (2021). Automatic detection of the thermal electron density from the WHISPER experiment onboard CLUSTER-II mission with neural networks. *Journal of Geophysical Research: Space Physics*, *126*(3), e2020JA028901. <https://doi.org/10.1029/2020JA028901>
- González-Casado, G., Juan, J. M., Sanz, J., Rovira-García, A., & Aragón-Angel, A. (2015). Ionospheric and plasmaspheric electron contents inferred from radio occultations and global ionospheric maps. *Journal of Geophysical Research: Space Physics*, *120*(7), 5983–5997. <https://doi.org/10.1002/2014JA020807>
- Guerra, M. (2026). GFLC for GNSS observables derived from the LuGRE mission. *Zenodo*. [Dataset]. <https://doi.org/10.5281/zenodo.18890330>
- Halekas, J. S., Poppe, A. R., Harada, Y., Bonnell, J. W., Ergun, R. E., & McFadden, J. P. (2018). A tenuous lunar ionosphere in the geomagnetic tail. *Geophysical Research Letters*, *45*(18), 9450–9459. <https://doi.org/10.1029/2018GL079936>
- Huddleston, M. M., Chappell, C. R., Delcourt, D. C., Moore, T. E., Giles, B. L., & Chandler, M. O. (2005). An examination of the process and magnitude of ionospheric plasma supply to the magnetosphere. *Journal of Geophysical Research*, *110*(A12), A12202. <https://doi.org/10.1029/2004JA010401>
- Hysell, D. L., Milla, M. A., & Woodman, R. F. (2017). High-altitude incoherent-scatter measurements at jicamarca. *Journal of Geophysical Research: Space Physics*, *122*(2), 2292–2299. <https://doi.org/10.1002/2016JA023569>
- Iiyama, K., & Gao, G. (2025). Ionospheric and plasmaspheric delay characterization for lunar terrestrial GNSS receivers with global core plasma model. *arXiv preprint arXiv:2510.10059*. <https://doi.org/10.48550/arXiv.2510.10059>
- Jakowski, N., & Hoque, M. M. (2018). A new electron density model of the plasmasphere for operational applications and services. *Journal of Space Weather and Space Climate*, *8*, A16. <https://doi.org/10.1051/swsc/2018002>
- Jin, S., Gao, C., Yuan, L., Guo, P., Calabria, A., Ruan, H., & Luo, P. (2021). Long-term variations of plasmaspheric total electron content from topside GPS observations on LEO satellites. *Remote Sensing*, *13*(4), 545. <https://doi.org/10.3390/rs13040545>
- Kashcheyev, A., & Nava, B. (2019). Validation of NeQuick 2 model topside ionosphere and plasmasphere electron content using COSMIC POD TEC. *Journal of Geophysical Research: Space Physics*, *124*(11), 9525–9536. <https://doi.org/10.1029/2019JA026971>
- Kitamura, N., Shinbori, A., Nishimura, Y., Ono, T., Iizima, M., & Kumamoto, A. (2009). Seasonal variations of the electron density distribution in the polar region during geomagnetically quiet periods near solar maximum. *Journal of Geophysical Research*, *114*(A1). <https://doi.org/10.1029/2008JA013288>
- Kumamoto, A., Tsuchiya, F., Kasahara, Y., Kasaba, Y., Kojima, H., Yagitani, S., et al. (2018). High frequency analyzer (HFA) of plasma wave experiment (PWE) onboard the arase spacecraft. *Earth Planets and Space*, *70*(1), 1–14. <https://doi.org/10.1186/s40623-018-0854-0>
- Lotko, W. (2007). The magnetosphere-ionosphere system from the perspective of plasma circulation: A tutorial. *Journal of Atmospheric and Solar-Terrestrial Physics*, *69*(3), 191–211. <https://doi.org/10.1016/j.jastp.2006.08.011>
- Matzka, J., Bronkalla, O., Tornow, K., Elger, K., & Stolle, C. (2021). Geomagnetic Kp index. V. 1.0. *GFZ Data Services*. [Dataset]. <https://doi.org/10.5880/Kp.0001>
- Menk, F., Kale, Z., Sciffer, M., Robinson, P., Waters, C., Grew, R., et al. (2014). Remote sensing the plasmasphere, plasmopause, plumes and other features using ground-based magnetometers. *Journal of Space Weather and Space Climate*, *4*, A34. <https://doi.org/10.1051/swsc/2014030>
- Minetto, A., Dovis, F., Nardin, A., Vouch, O., Impresario, G., Musmeci, M. (2022). Analysis of GNSS data at the Moon for the LuGRE project. In *2022 IEEE 9th international workshop on metrology for AeroSpace (MetroAeroSpace)* (pp. 134–139). <https://doi.org/10.1109/MetroAeroSpace54187.2022.9855945>
- Miyoshi, Y., Shinohara, I., Takashima, T., Asamura, K., Higashino, N., Mitani, T., et al. (2018). Geospace exploration project ERG. *Earth Planets and Space*, *70*(1), 101. <https://doi.org/10.1186/s40623-018-0862-0>

- Padokhin, A. M., Chernyshov, A. A., Andreeva, E. S., Nazarenko, M. O., Andreevsky, S. E., & Mogilevsky, M. M. (2025). Tomographic methods for studying the upper atmosphere and near-Earth space: Current state and development prospects. *Cosmic Research*, *63*(3), 284–304. <https://doi.org/10.1134/S0010952525601392>
- Parker, J. J. K., Dovis, F., Anderson, B., Ansalone, L., Ashman, B., Bauer, F. H., et al. (2022). The lunar GNSS receiver experiment (LuGRE). In *Proceedings of the 2022 international technical meeting of the institute of navigation* (pp. 420–437). <https://doi.org/10.33012/2022.18199>
- Parker, J. J. K., Dovis, F., Pozzobon, O., Facchinetti, C., Anderson, B., Ansalone, L., et al. (2025). Lunar GNSS receiver experiment (LuGRE) mission data (version v1). *Zenodo*. [Dataset]. <https://doi.org/10.5281/zenodo.16411687>
- Parker, J. J. K., Dovis, F., Konitzer, L., Esantsi, N., Ashman, B., Minetto, A., et al. (2026). GNSS reception at the moon: First results of the lunar GNSS receiver experiment (LuGRE). *NAVIGATION: Journal of the Institute of Navigation*, *73*(1), navi.756. <https://doi.org/10.33012/navi.756>
- Pignalberi, A., Nava, B., Prol, F., Haralambous, H., Themens, D. R., Smirnov, A., et al. (2025). Improving the NeQuick model in the plasmasphere through radio occultation and POD TEC observations. *IEEE Transactions on Geoscience and Remote Sensing*, *63*, 1–19. <https://doi.org/10.1109/TGRS.2025.3635770>
- Rawer, K. (2013). *Wave propagation in the ionosphere* (Vol. 5). Springer Science & Business Media.
- Ripoll, J.-F., Pierrard, V., Cunningham, G. S., Chu, X., Sorathia, K. A., Hartley, D. P., et al. (2023). Modeling of the cold electron plasma density for radiation belt physics. *Frontiers in Astronomy and Space Sciences*, *10*, 1096595. <https://doi.org/10.3389/fspas.2023.1096595>
- Smirnov, A., Shprits, Y., Lühr, H., Kronberg, E. A., Goldstein, J., Miyoshi, Y., et al. (2025). Bridging the gap between the earth's ionosphere and plasmasphere. *Geophysical Research Letters*, *52*(23), e2025GL119267. <https://doi.org/10.1029/2025GL119267>
- Usanova, M. E., & Shprits, Y. Y. (2017). Inner magnetosphere coupling: Recent advances. *Journal of Geophysical Research: Space Physics*, *122*(1), 102–104. <https://doi.org/10.1002/2016JA023614>
- Ventriglia, V., Guerra, M., & Ghidoni, R. (2026). Iono-LuGRE (version 0.1.2). *Zenodo*. [Software]. <https://doi.org/10.5281/zenodo.19127819>
- Watanabe, S., Bilitza, D., Tsuchiya, F., Kumamoto, A., Miyoshi, Y., Kasahara, Y., et al. (2025). Satellite observations and modeling of the plasmopause structure and dynamics. *Advances in Space Research*, *75*(5), 4230–4244. <https://doi.org/10.1016/j.asr.2024.10.015>
- Wu, M. J., Guo, P., Xu, T. L., Fu, N. F., Xu, X. S., Jin, H. L., & Hu, X. G. (2015). Data assimilation of plasmasphere and upper ionosphere using COSMIC/GPS slant TEC measurements. *Radio Science*, *50*(11), 1131–1140. <https://doi.org/10.1002/2015RS005732>
- Zhelavskaya, I. S., Shprits, Y. Y., & Spasojević, M. (2017). Empirical modeling of the plasmasphere dynamics using neural networks. *Journal of Geophysical Research: Space Physics*, *122*(11), 11227–11244. <https://doi.org/10.1002/2017JA024406>